EES Solar

ROYAL SOCIETY OF CHEMISTRY

PAPER

View Article Online
View Journal

Cite this: DOI: 10.1039/d6el00076b

# A new era in solar fuels: a battery pushes PV-driven $CO_2$ reduction beyond its limits

Thérèse Cibaka,[ad] Tsvetelina Merdzhanova,[*a] Oleksandr Astakhov,[a] Robert Zandonella,[b] Sergey Shcherbachenko,[ac] Paul Paciok,[b] Marc Heggen,[b] Rafal Dunin-Borkowski,[b] Christoph Brabec[ae] and Peter Strasser[d]

Photovoltaic (PV) technologies are central to renewable energy generation, yet their intermittent output limits efficient utilization and grid integration. Coupling PV with short- and long-term energy storage at the earliest stage of electricity generation is an attractive but challenging strategy for stabilizing PV output. Using batteries is a feasible way to cover short-term PV output variations. For longer, seasonal variations, an electrochemical (EC) pathway to produce fuels and chemicals is a promising solution. Here, we demonstrate a self-sufficient directly coupled hybrid PV-battery-electrochemical $CO_2$ reduction (PV-B-EC) system that autonomously and continuously converts PV energy to fuels under realistic daily irradiance and temperature variations. In comparison with a directly coupled PV-EC reference, the PV-B-EC storage combination is capable of covering timescales ranging from seconds to years. This is achieved while operating efficiently without the need for control electronics. Furthermore, the PV-B-EC combination stabilises the $CO_2$ reduction process by minimising power peaks. In our experiment, the system with a battery achieved near-ideal energy coupling efficiency (0.99 *vs.* 0.96), higher electrochemical voltage efficiency (57.8% *vs.* 47%), and a $2.3\%_{\text{abs.}}$ increase in solar-to-chemical efficiency, exceeding even the theoretical limit of the equivalent reference PV-EC system. These results validate a previously predicted synergistic efficiency enhancement arising from the redistribution of photovoltaic energy through the battery. Implications of the power input stabilization provided by the battery on the Ag catalyst structure are studied in a dedicated experiment involving scanning transmission electron microscopy (STEM) in combination with energy-dispersive X-ray spectroscopy (EDX) and 4D-STEM analyses. For the tested voltage profiles, no discernible differences in microstructural features were observed between the PV-B-EC and PV-EC reference systems. The findings demonstrate that the simple addition of a Li-ion battery substantially enhances the PV-to-fuel efficiency under realistic field conditions, offering a simple and scalable route towards stable and efficient solar-driven $CO_2$ conversion.

Received 28th April 2026
Accepted 30th April 2026

DOI: 10.1039/d6el00076b

rsc.li/EESSolar

## Broader context

Global warming is accelerating the need to decarbonize energy systems across all sectors, including hard-to-abate applications such as transportation. While renewable electricity from photovoltaics (PV) is central to this transition, increasing PV penetration is already exposing fundamental limitations in grid flexibility. These limitations lead to growing curtailment of solar electricity, not because of an oversupply of energy, but due to short-term power peaks that exceed grid capacity. Grid expansion can increase allowable peak power but does not necessarily improve the utilization of renewable energy and entails significant economic and societal costs. As a result, complementary strategies are required that enable the capture and use of curtailed PV electricity through local conversion or long-term storage directly at the point of generation. Using batteries is a feasible way to cover short-term PV output variations. For longer, seasonal variations, an electrochemical (EC) pathway to produce fuels and chemicals is a promising solution.

## Introduction

Photovoltaics are one of the primary contributors to renewable energy, their rapid growth is promising for accelerating the green energy transition.[1] Due to daily and seasonal fluctuations, photovoltaic power capacity often exceeds the immediate demand and capabilities of the grid, or is unavailable when irradiance is low. This mismatch leads to PV curtailment and

---

[a] *Forschungszentrum Jülich GmbH, IMD-3 Photovoltaik, Jülich, Germany*
[b] *Forschungszentrum Jülich GmbH, Ernst-Ruska, Jülich, Germany*
[c] *Jülich Aachen Research Alliance (JARA-Energy) and Faculty of Electrical Engineering and Information Technology, RWTH Aachen University, Aachen, Germany*
[d] *Technical University of Berlin, Institute of Chemistry, Berlin, Germany*
[e] *Friedrich-Alexander-Universität Erlangen-Nürnberg - Materials for Electronics and Energy Technology (i-MEET), Helmholtz-Institute Erlangen-Nürnberg (HI ERN), Germany*

grid instabilities once PV generation gains significant share[2–4] and may become a major challenge for national and international grids in the near future. The temporal generation-demand mismatch must be mitigated by storage solutions that capture excess generation capacity. To cover the entire spectrum of variability, these storage solutions must operate on a wide range of timescales, from seconds to years. Ideally, storage should be coupled with PV at the earliest point of generation, before DC-AC conversion and feeding into the grid. This PV-storage architecture minimizes infrastructure demands at the PV system and grid levels while maximizing PV capacity utilization. Battery technology is most versatile and suitable for short term energy storage[5] on the DC side of PV systems. Batteries integrated at the PV module[6,7] or system level[5] are expected to store energy equivalent to several hours of nominal PV output,[8] which in practice can mitigate generation-demand mismatch on a timescale of 1–2 days. In seasonal or yearly time frames, the most promising way of capturing unutilized PV capacity is the conversion of PV electricity into solar fuels by electrochemical (EC) reactors producing chemicals, such as hydrogen *via* water splitting[9–13] or hydrocarbons *via* electrochemical $CO_2$ reduction.[14–18] The latter process of $CO_2$ reduction is of particular interest because of industry decarbonization and variety of potential products. To avoid ambiguity, it should be noted that the electrochemical cell or reactor referred to in this study specifically denotes an electrocatalytic cell.

Combining batteries (B) and electrochemical cells (EC) to create PV-B-EC systems could be the ultimate solution for absorbing PV's intermittent DC power and stabilising its output for connection to the grid. This would facilitate the smooth and virtually unlimited integration of PV generation into energy systems. Batteries and electrolysers are typically connected to photovoltaics *via* power electronics, with multiple DC-AC-DC conversions of electric power in some cases.[9,11,19–22] However, it was pointed out in a number of publications that power electronics are actually not necessary when PV is coupled to batteries or electrochemical cells,[23–27] and properly combined components allow efficient operation of PV-EC[28–33] or PV-B[6,24,26,27,34–38] systems under realistic variations in irradiance and PV-module temperature. Additionally, direct coupling of PVs to EC devices has demonstrated the potential for efficient self-sustained operation[20,30–32,39–43] and the highest solar-to-chemical (STC) efficiencies.[29,32,39,40,42–45]

In our previous work, we investigated PV-B-EC systems with water-splitting electrolysers under direct coupling. We demonstrated self-sustaining operation in idealised day–night cycles, with the battery enabling high-power coupling during the day and extending EC operation into the night.[46,47] Beyond the expected stabilising effects, we showed both theoretically and experimentally that PV-B-EC systems achieve a synergistic gain in solar-to-hydrogen (STH) efficiency compared to PV-EC references without a battery.[46–48] This gain arises because the battery shifts part of the daytime energy to nighttime operation, reducing electrolyser current densities, power demand and thus kinetic overpotential losses. Notably, even after accounting for battery losses, total system losses are lower than in the battery-free case.[46,47] Most recently, we demonstrated that in a basic day–night cycle, an optimally coupled PV-B-EC system can surpass the theoretical STH limit of the corresponding optimally coupled reference system without a battery.[48] In this work, we take the next step by exploring the potential of PV-B-EC systems to operate with a $CO_2$ electrolyser under realistic PV generation profiles, reflecting typical solar irradiance and module temperature. The 2022 $CO_2$ reduction roadmap identifies CO as a strategic target, serving as a key building block for numerous industrially relevant processes.[45] Accordingly, this study focuses on CO as the primary product of $CO_2$ reduction, with $H_2$ from the hydrogen evolution reaction (HER) considered as a valuable by-product.

In this work, a parallel-connected photovoltaic–electrochemical cell system (PV-EC) and a parallel-connected photovoltaic–battery–electrochemical cell (PV-B-EC) were respectively tested under a double day and single night cycle. Daytime reproduced an accelerated summer day in Golden Colorado USA. For dynamic changes of irradiance and temperature conditions and photovoltaic design flexibility, we utilised an emulation tool, a computer-based algorithm run by a source measure unit, able to reproduce any IV characteristics of any photovoltaics under any irradiance and temperature conditions.[49] While this protocol provides an accelerated representation of diurnal operation, it should be regarded as an emulation rather than a demonstration of long-term, real-world performance; accordingly, long-term degradation, battery cycling stability, and weather variations are not explicitly addressed. Instead, the focus is on demonstrating the feasibility and key operational aspects of self-sustained $CO_2$ reduction under dynamically coupled photovoltaic conditions using a laboratory-scale reactor. This approach brings field to the lab and enables fast and realistic screening of catalyst materials, representing a necessary step prior to outdoor validation and upscaling. For straightforward comparison between PV-EC and PV-B-EC, the emulated PV always displayed identical attainable maximum daily energy output when connected to EC or B-EC, the same EC was utilised in the two system configurations. Under realistic field irradiance and temperature conditions, PV-EC operation experiences natural fluctuations in irradiance that induce corresponding variations in the EC operating voltage, resulting in a dynamic voltage regime. The addition of a battery stabilises the EC operating voltage and, as a result, the operating current of the EC device, even during dark periods. In the PV-EC system, the EC operated only during daytime, powered directly by PV. In contrast, in the PV-B-EC system, the PV supplied power to the EC and simultaneously charged the battery during daytime, while the battery sustained EC operation during nighttime. Herein, we show that under realistic irradiance and temperature fluctuations, our PV-EC system achieves high solar-to-chemical efficiency and tolerates up to a fivefold variation in current density. Notably, the simple addition of a battery further enhances the coupling factor while reducing overpotential, thereby improving STC performance. In addition to the device performance, a detailed study of the impact of the two distinct operating regimes on the Ag catalyst was analysed using STEM and 4D-STEM.

## Experimental section

### PV module

The time series of IVs representing the target 'day' was generated using the IV characteristics of a silicon heterojunction (SHJ) solar cell[50] measured under different combinations of irradiance and temperature, with irradiance (G) ranging from 0.2 to 1.1 sun and temperature (T) varying between 25 °C and 60 °C. For the $CO_2RR$, the SHJ solar cell was virtually converted into a 46.22 $cm^2$ PV module for optimum coupling to the loads (EC or B-EC).

### Battery

The battery utilized in this study is a commercial lithium-ion based with 1.3 Ah capacity and 2.4 V nominal voltage, with a 1.5–2.85 V voltage range. Charge–discharge curves presented in Fig. S1 in the SI were measured with an Origalys OGF 05A potentiostat at C ratings of 0.1, 0.25, 0.5 and 1. From these curves, current voltage characteristics of the battery at states of charge (SOCs) of 10%, 30%, 50%, 70% and 90% were calculated and are shown in Fig. S2 in the SI. In order to maintain EC operation at meaningful working current and voltage during the "day" and "night" cycle, PV-B-EC operated with the battery at 70% SOC at the beginning of the cycle.

### Electrochemical cell

The electrochemical $CO_2$ reduction reaction ($CO_2RR$) was conducted in a microflow electrochemical cell (EC) commercially available from Electrocell. The preparation of the silver-based gas diffusion electrode (Ag-GDE, cathode) and a schematic of the EC cell performing $CO_2$ reduction at the Ag-GDE and oxygen evolution at the anode ($IrO_2$ bulk plate provided by the EC manufacturer) is presented in the SI (Fig. S3). The anolyte and catholyte are both $CO_2$-saturated solutions of 1 M $KHCO_3$ ($KHCO_3$ salt, Sigma Aldrich). In addition to the $CO_2$ dissolved in the electrolyte, $CO_2$ flows through the GDE. The Ag-GDE cathode, which has an area of 9.5 $cm^2$, was prepared with homogeneous and high coverage of silver on the GDE to enhance CO selectivity. Cathode and anode compartments were separated with Selemion, an anion exchange membrane that allows hydroxide ions diffusion from the cathode to the anode. Catholyte and anolyte reservoirs were in-house built Teflon cups, with a volume capacity of 100 mL, equipped with liquid and gas inlet and outlet connections and a built-in temperature sensor. EC operations were sustained at 45 °C by heating all electrolyte tubing using heat pipes (HilleSheim, HT 60). Gas products, along with unreacted $CO_2$, were analyzed using online gas chromatography (Shimadzu GC 30301) at 15-minute intervals. Prior to measurements, the GC was calibrated with an internal three-point calibration curve, established through two-fold serial dilutions of a reference gas (Linde, purity 5.6) composed of 96% He, 1% $H_2$, 1% CO, 1% $CH_4$, and 1% $CO_2$. These dilutions were prepared by blending the reference gas with high-purity He (Linde, 5.6).

### Microstructure analysis of silver nanoparticles under constant and dynamic voltage conditions

Following the assessment of electrochemical performance in the PV-EC and PV-B-EC configurations, we conducted a dedicated experiment to evaluate the effect of fluctuating *versus* constant applied voltage on the micro and nanostructure of silver nanoparticles. For this, silver nanoparticles were deposited on three TEM finder grids (grid 1, grid 2 and grid 3): grid 1 coated with the reference pristine Ag, grid 2 with Ag destined to the $CO_2$ reduction reaction ($CO_2RR$) under dynamic applied voltage and grid 3 with Ag for the $CO_2RR$ under constant stable applied voltage. The TEM finder grids (S147A9, Plano) were prepared by spraying a solution containing approximately 0.1 mg of silver nanoparticles, 1 mL of ultrapure water (resistivity 18.2 MΩ cm), and 0.5 mL of HPLC-grade propanol. The grids were then allowed to air-dry.

### Ag-coated TEM grid cathode preparation

To employ an Ag-coated grid in electrochemical operation ensuring mechanical stability, the grid was mounted in a sandwich-like configuration comprising a nylon grid without carbon coating (418CN-MB, SPI Supplies), two M2 stainless steel washers, and titanium reverse-action tweezers (N5TI, Dumont). Prior to assembly, all components were sequentially cleaned by ultrasonication in isopropyl alcohol and ultrapure water, followed by plasma cleaning (MCA Chamber, ibss Group Inc). Assembly was performed by placing the Ag-coated grid over the aperture of the first washer with the carbon film facing upward, followed by placement of the nylon grid to contact the carbon film and a second washer to complete the sandwich-like structure. The assembled configuration was directly used as the cathode during $CO_2RR$ experiments.

### $CO_2$ reduction using a Ag-coated TEM grid cathode

To investigate the effect of different operating profiles on Ag nanoparticles, Ag-coated TEM grid cathodes were employed in a dedicated $CO_2$ reduction experiment. The reaction was carried out at room temperature and atmospheric pressure in a custom-built H-cell, conditions selected to minimize mechanical and thermal stress on the TEM grid carbon film. The cell was separated by a glass frit and equipped with a fixed Luggin capillary. A graphite rod was used as the counter electrode, while the cathodic compartment contained a hydrogen reference electrode (Hydroflex, Gaskatel) and inverted tweezers holding the Ag-TEM grid cathode. Both compartments were filled with 110 mL of $CO_2$-saturated 1 M $KHCO_3$ and stirred at 330 rpm (Variomag micro, Thermo Scientific). The Ag-TEM grid cathode was immersed immediately prior to applying the potential sequence, with the carbon film oriented toward the counter electrode.

Dynamic PV-EC operation was simulated by applying a sequence of 11 consecutive potentials *versus* RHE (−0.52, −0.58, −0.64, −0.70, −0.76, −0.78, −0.76, −0.70, −0.66, −0.58, and −0.52 V), each held for 54.5 s. Stabilized PV-B-EC operation was simulated on a separate Ag-TEM grid cathode by applying a constant potential of −0.58 V *versus* RHE for 10 min. These potential profiles correspond to those experienced by the Ag gas-diffusion electrode under the respective PV-EC and PV-B-EC operating conditions. All potentials were applied using a potentiostat (SP-50, BioLogic) controlled by EC-Lab software (v11.20), with current recorded without iR compensation.

### Electron microscopy characterization

All three Ag-coated TEM grids (grid 1 with pristine Ag, grid 2 with Ag after the $CO_2RR$ under dynamic applied voltage and grid 3 with Ag after the $CO_2RR$ under stable applied voltage) were characterized using a probe-corrected Hitachi HF5000 scanning transmission electron microscope. High-resolution (HR) mapping was performed using aperture C2-4 in EELS1 mode, with a convergence angle of 21 mrad and a beam current of 9 μA. Imaging was carried out using an on-axis dark-field detector, complemented by secondary electron imaging to assess surface topology. Energy-dispersive X-ray spectroscopy (EDX) line scans were acquired using an Ultim Max TLE detector (Oxford). Representative acquisition parameters (line scan spot 10) included a magnification of 80 000×, 2048 energy channels over a 20 keV range (10 eV per channel), 200 points per line, 400 passes, a pixel dwell time of 2 ms, and eight accumulated lines. Pulse pile-up correction was applied during acquisition. The 4D-STEM investigation was performed with a Tescan Tensor STEM using beam precession and 100 kV accelerating voltage. Diffraction pattern matching was performed with Tescan's in-house software "Explore"; cif files were downloaded from https://next-gen.materialsproject.org/.

### Field profiles of PV module irradiance and temperature

Realistic irradiance and temperature conditions were established by analyzing available NREL data set of a silicon heterojunction PV module installed in Golden, Colorado-USA, operating during one year.[51,52] Fig. 1a displays the cumulative energy of that installed PV module over a combination of irradiance and temperature during that year in Golden. To design a representative summer day, we selected a set of eleven irradiance (G) and temperature (T) combinations that allowed for high PV energy. These eleven G and T pairs are highlighted with green circles in Fig. 1a.

To accurately evaluate and compare PV-EC and PV-B-EC operation under irradiance and temperature variations during the daytime, as well as day–night cycles, we designed two identical "days", each lasting one hour, separated by a long "night" of nearly two hours, as illustrated in Fig. 1b. Each day was composed of a succession of the selected eleven G and T pairs in Fig. 1a. Unlike typical summer conditions, our designed night-time was longer than the daytime to ensure sufficient time for the battery to supply EC with the solar energy stored during the day.

### Power and energy coupling optimization

In a simple generator-load circuit, the power generated by the source equals the power consumed by the load at every instant. In other terms, when a generator and a load are directly coupled, the operating point (OP) of the system is defined by the intersection of their respective current–voltage ($I$–$V$) characteristic curves. This operating point is characterised by an operating current ($I_{OP}$) and an operating voltage ($V_{OP}$), whose product defines the operating power ($P_{OP}$), as shown in eqn (1).

$$P_{OP} = V_{OP} \times I_{OP} \tag{1}$$

For a photovoltaic (PV) generator, the maximum power that can be delivered corresponds to the maximum power point (MPP) of its $I$–$V$ curve and is denoted as $P_{MPP}$. At any given time, the degree of power coupling between a PV generator and a load is quantified by the power coupling factor, $C$, defined as the ratio between the maximum power available from the PV device and the actual operating power of the coupled system, as shown in eqn (2):

$$C = P_{OP}/P_{MPP} \tag{2}$$

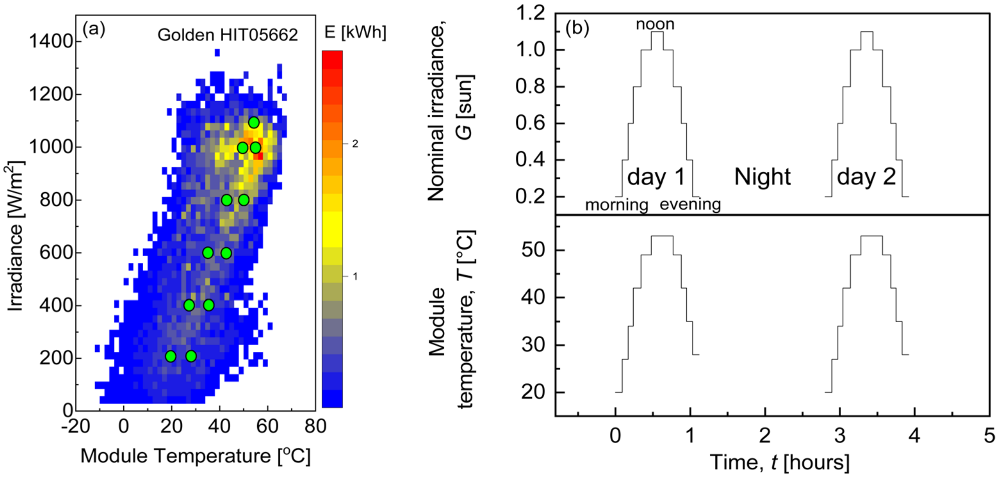

Fig. 1 (a) One-year cumulative energy of an installed Si-PV (Golden, Colorado – USA) plotted against irradiance and temperature. Eleven green circles represent the selected G and T combination to design a typical summer day. (b) Realistic ambient condition design mimicking two typical summer days separated by one long night using the eleven selected irradiance and temperature combinations.

A value of $C = 1$ indicates ideal power matching, where the system operates exactly at the maximum power point of the PV, while deviations from unity reflect suboptimal power coupling.

When the power input is intermittent, the power coupling factor, which reflects performance at a single point in time, may not fully capture the overall coupling behavior during extended operation. For this reason, it is more appropriate to assess the energy coupling factor, defined as the ratio between the energy consumed by the EC and the maximum energy the PV system could have supplied over the same time interval. The solar-to-chemical efficiency, STC, is then the product of photovoltaic efficiency, electrochemical cell efficiency and the coupling factor.

$$\mathrm{STC} = \eta_{\mathrm{PV}} C \eta_{\mathrm{EC}} \tag{3}$$

where photovoltaic efficiency ($\eta_{\mathrm{PV}}$) is defined as the fraction of incident solar irradiance on the PV surface that is converted into electrical power at the maximum power point, and EC efficiency ($\eta_{\mathrm{EC}}$) denotes the fraction of the applied electrical power (voltage × current) that is effectively converted into desired chemical products.

In both PV-EC and PV-B-EC scenarios, we utilized current–voltage characteristics of two equivalent photovoltaic modules based on silicon heterojunction (SHJ) solar cells with the same total area and power conversion efficiency (PCE). PV devices were mathematically designed to optimally match the characteristics of the EC or B-EC under dynamic conditions at 1.1 sun and 53.3 °C. To ensure equal power density across both operations, the equivalent PV devices retained a fixed total area of 46.22 cm$^2$. Fig. 3 in the Results and discussion section shows PV maximum power matching with EC and PV maximum power matching with B-EC in current–voltage graphs and power–voltage graphs. For the PV-EC operation, the PV system consisted of a module with 5.25 serially connected cells (equivalent to 525 cell PVs connected to 100 electrochemical cells), with each cell having an area of 8.81 cm$^2$. For the PV-B-EC scenario, the PV system consisted of a module with 4.25 serially connected cells, each with an area of 10.87 cm$^2$.

### PV-EC and PV-B-EC experiments with hardware-emulated photovoltaics

Under laboratory conditions, PV-driven operations are typically conducted with photovoltaics illuminated at 1 sun AM1.5 G and a controlled temperature of 25 °C using a sun simulator. This setup however presents insufficient dynamic irradiance (G) and temperature (T) flexibility and long-time irradiance and spectral stability. The dynamic variation of irradiance–temperature combinations simulating a summer day, along with the flexibility of PV current–voltage characteristics, is achieved using a dedicated PV emulator. This emulator is a computer-driven algorithm that controls a source measurement unit, which in turn replicates the IV characteristics of PV devices of any type, size, and number of cells under the specified irradiance and temperature conditions. The PV emulator developed for this study reproduce PV IV characteristics with precision and accuracy comparable to that of a AAA-class solar simulator.[49] The time series of IVs representing the target ‘day’ was generated using the IV characteristics of an in-house fabricated 246.21 cm$^2$ SHJ solar cell. The specific sequence of irradiance and temperature representing the sunny day profile is shown in Table S1 in the SI.

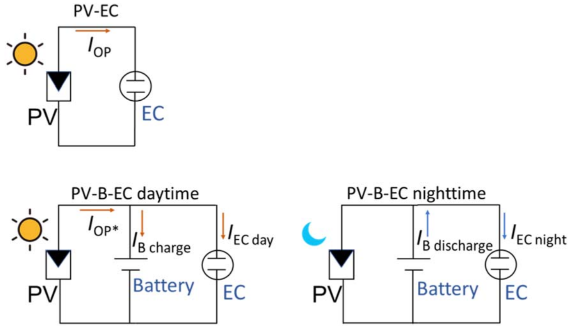

Fig. 2 Electrical circuit of PV-EC operation and PV-B-EC during both daytime and nighttime.

### PV-EC and PV-B-EC configurations

With PV-EC operation, EC is directly connected to the source measure unit (SMU) emulating the PV. The operating voltage ($V_{\mathrm{OP}}$) and current ($I_{\mathrm{OP}}$) are recorded using a Keithley SMU. With PV-B-EC operation, all three devices are connected in parallel and B-EC is connected to the PV in a four-wire configuration to account for voltage losses in the cables. During daytime, operations are mostly powered by emulated-PV *via* the SMU, which records operating current ($I_{\mathrm{OP*}}$) and voltage ($V_{\mathrm{OP*}}$) of B-EC. To assess specific current and voltage of the battery, a data logger located at the connection to the battery measured and recorded both $V_B$ and $I_B$.

Fig. 2 shows the electrical circuit operation of both systems (PV-EC and PV-B-EC) in terms of the current.

PV-B-EC daytime: $V_{\mathrm{OP*}} = V_{\mathrm{B}} = V_{\mathrm{EC}}$

$$I_{\mathrm{OP*}} = I_{\mathrm{B\ charging}} + I_{\mathrm{EC\ day}}$$

PV-B-EC nighttime: $V_{\mathrm{B}} = V_{\mathrm{EC}}$

$$I_{\mathrm{B\ discharging}} = I_{\mathrm{EC\ night}}$$

The system efficiency including equations for PV conversion, EC, and solar-to-chemical efficiencies are provided in the SI.

## Results and discussion

### Power coupling optimization for PV-EC and PV-B-EC

Two equivalent photovoltaic (PV) devices, each with the same maximum power, were designed for optimal power coupling with their respective loads, EC or B-EC, under 1 sun and 49 °C conditions, corresponding to the irradiance (G) and temperature (T) with the highest PV energy during the simulated day.

Fig. 3a presents the PV-EC and PV-B-EC coupling in terms of current–voltage ($I$–$V$) characteristics. The black curve represents the PV, the blue line denotes the battery's $I$–$V$ characteristic at 70% SOC, the EC is shown by the blue curve, and the combined

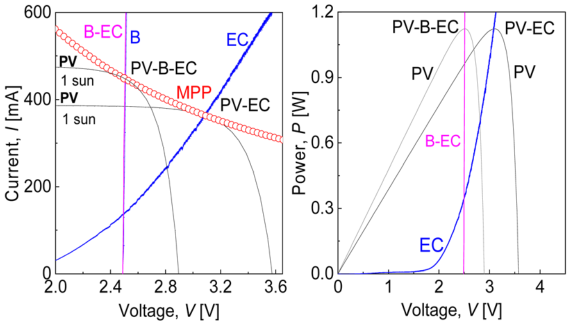

Fig. 3 (a) Current–voltage and (b) power–voltage characteristics of PV (1 sun), EC, B and B-EC. For each scenario, photovoltaic has been adjusted for optimal coupling with EC (in the PV-EC setup) and with B-EC (in the PV-B-EC setup). The red circles represent identical PV maximum power points with different voltages and currents.

EC-B system is shown in pink. Charge–discharge curves and current–voltage characteristics of the battery at different SOCs are available in Fig. S1 and S2 in the SI. Batteries typically exhibit very low internal resistance, resulting in an *I*–*V* curve that is nearly parallel to the current axis. When an electrochemical cell (EC) is connected in parallel with a battery (B), the combined *I*–*V* characteristic becomes dominated by the battery's behavior, closely resembling its nearly vertical profile. The red circles represent the set of current–voltage points with equal maximum power (1.12 W) for equivalent photovoltaics with varying configurations of cell count and cell area. A more detailed description of the approach to PV scaling and power coupling optimization for a very similar case of equivalent PV-EC and PV-EC-B systems can be found in the study by Chibuko *et al.*, 2025.[48] Fig. 3a shows the power–voltage (*P*-–*V*) curves of the equivalent PVs (black lines), which exhibit identical maximum power values but at different voltages. The corresponding load power–voltage characteristics align at these points: The B-EC curve (pink) reaches PV maximum power at $V_{\mathrm{MPP}} = 2.5$ V, while the EC curve (blue) matches with PV maximum power at $V_{\mathrm{MPP}} = 3.1$ V.

## Comparison of PV-EC and PV-B-EC operation over a double-day, single night cycle

The current–voltage (*I*–*V*) characteristics of the PV under the 11 selected irradiance (G) and temperature (T) conditions representing "daytime" are plotted in grey in Fig. 4a. The PV maximum power points are indicated by red hollow circles for the PV-EC configuration and red hollow squares for the PV-B-EC configuration. In the PV-EC configuration (Fig. 4a), the operating points (OP), shown as blue dots along the PV *I*–*V* curves, shift toward higher voltages under each tested condition. Such voltage instabilities during EC operation have been previously reported in the literature.[53–55] As irradiance increases from 0.2 sun to 1.1 sun, both the operating current ($I_{\mathrm{OP}}$) and voltage ($V_{\mathrm{OP}}$) rise from 67 mA to 335 mA and from 2.24 V to 3.24 V, respectively. In the PV-B-EC configuration (Fig. 4a), the B-EC operating points (OP*) are represented by purple dots along the PV *I*–*V* curves. During the morning hours, OP*$_{\mathrm{(day)}}$ points lie close to the B-EC *I*–*V* characteristic. From noon to evening, they gradually shift away from the initial B-EC curve due to the substantial increase in the battery's state of charge (SOC) as the PV system continuously charges it. Because the battery has a very low internal resistance and acts as a voltage stabilizer, voltage fluctuations that typically occur during EC operation have a negligible impact on OP*$_{\mathrm{(day)}}$. As irradiance increases from 0.2 sun to 1.1 sun, the operating current ($I_{\mathrm{OP*(day)}}$) rises significantly from 83 mA to 444 mA, while the operating voltage ($V_{\mathrm{OP*(day)}}$) increases only slightly from 2.48 V to 2.54 V.

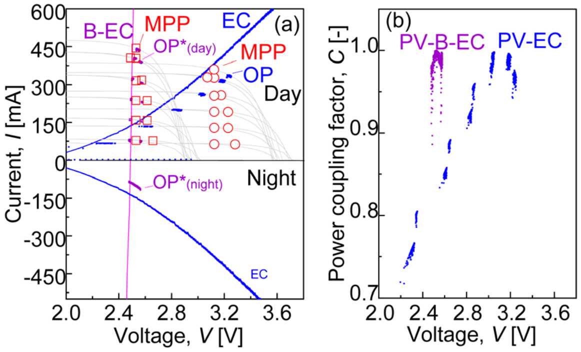

Fig. 4 PV-EC and PV-B-EC operating points during a double-day and single night cycle. (a) Current–voltage characteristics of the PV in grey, of the EC in blue and of the parallelly connected B-EC in purple. The maximum power points are red hollow circles for the PV connected to the EC and red hollow squares for the equivalent PV connected to the battery and EC, the operating points are blue dots aligned with PV IV curves for PV-EC and purple dots aligned with PV IV curves for PV-B-EC. For clarity, night operation is shown with negative currents, EC operating points are purple dots. (b) Power coupling factor of PV-EC and PV-B-EC over operating voltage.

During nighttime, when PV output is zero, the battery behaves as the only generator to EC. The operating points (OP*$_{\mathrm{(night)}}$) are related to EC night operation and are plotted with negative currents ($I_{\mathrm{OP*(night)}}$) for visual clarity. $V_{\mathrm{OP*(night)}}$ varies from 2.56 V to 2.48 V due to decreasing SOC as the battery discharged. As a result, the absolute value of $I_{\mathrm{OP*(night)}}$ decreased from 112 mA to 90 mA. The current values of EC$_{\mathrm{night}}$ are lower than those of the original EC polarization curve because of the cumulative operating voltage instabilities.

Fig. 4b compares the power coupling factors of the PV-EC and PV-B-EC configurations. The PV-EC coupling factor varies between 0.75 and 1, indicating less consistent power matching. In contrast, the PV-B-EC coupling factor remains high and nearly constant, with only slight variation between 0.95 and 1. The inclusion of the battery enables the B-EC system to more effectively utilize the available photovoltaic power, thereby enhancing the overall system efficiency.

## Battery operation in PV-B-EC configurations over a double-day, single night cycle

The low internal resistance of the battery limits voltage fluctuations, even under substantial changes in charging or discharging current. As shown in Fig. 5, the battery voltage remains nearly constant (2.48–2.54 V) despite an approximately six-fold variation in current. In the PV-B-EC configuration, the

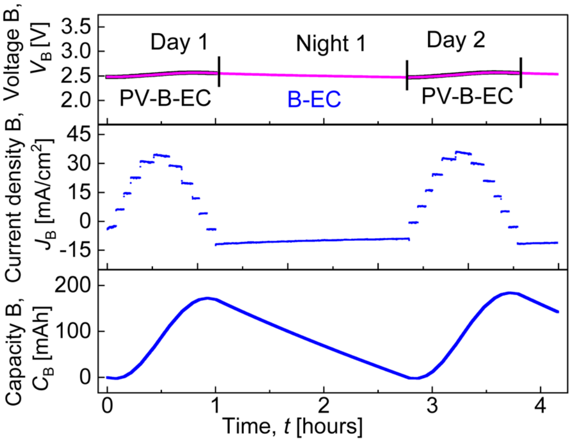

Fig. 5 Temporal evolution of battery operating voltage $V_B$, current density $J_B$ and capacity during a simulated accelerated double-day, single night cycle.

battery stabilizes the operating voltage ($V_{OP*}$) of the parallelly connected B-EC, which is consistent with our earlier observations.[46–48] During daytime on both day 1 and day 2, the battery current closely follows the irradiance pattern shown in Fig. 1b. In contrast, the EC maintained a relatively low and constant current throughout the double day single night as shown in Fig. 6b. In PV-B-EC, B absorb most of the PV current–voltage fluctuation during daytime and power EC during nighttime with more steady current–voltage.

At low irradiance levels, during mornings, evenings, and nighttime, negative current values indicate battery discharge while supplying power to the EC. Between approximately 0.4 sun and 1.1 sun, the battery is charged by the PV, with charging currents ranging from 6 mA cm$^{-2}$ to 35 mA cm$^{-2}$. At the beginning of the PV-B-EC experiment, the battery was at 70% state of charge, allowing it to power the EC. Note that the performance evaluation of the PV-B-EC system considers only the energy generated by the PV; therefore, the initial battery contribution to the EC will be excluded from the overall system assessment. At the beginning of day 1, the battery capacity decreases slightly as it powers the EC, then increases to 174 mAh as it is recharged by the PV system until late in the day. By the end of day 1, under 0.2 sun, the battery begins discharging again to power the EC throughout the long night, during which all PV energy stored during the day is supplied to the EC. On day 2, the battery exhibits a similar behavior: a slight decrease in capacity in the early morning, followed by an increase toward the end of the day.

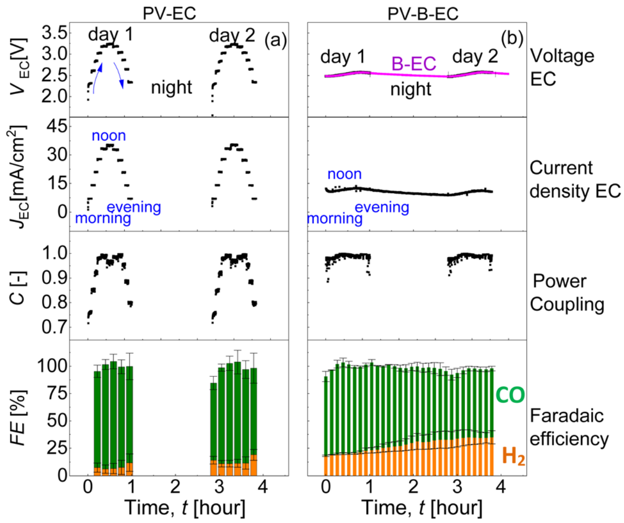

Fig. 6 (a) Temporal evolution of EC operating voltage $V_{EC}$, current density $J_{EC}$, coupling factor of PV-EC, and product faradaic efficiency during a simulated accelerated double-day, single night cycle. (b) Temporal evolution of EC operating voltage $V_{EC}$, current density $J_{EC}$, coupling factor of PV-B-EC, and product faradaic efficiency during a simulated accelerated double-day, single night cycle.

## EC operation in PV-EC and PV-B-EC configurations over a double-day, single night cycle

The experiments were first conducted using the PV-EC configuration over a two-day, single-night cycle, followed by the PV-B-EC configuration under another identical cycle. In both cases, the electrochemical cell was equipped with the same $IrO_x$ anode and Ag-GDE to minimize variability and isolate the effect of the system configuration. Both system configurations exhibited identical maximum attainable PV energy output. In the PV-EC system, the EC operates exclusively during daytime hours. In contrast, in the PV-EC-B, the addition of a battery enables EC operation to extend into the nighttime. Fig. 6 displays a comparison between EC operation in the PV-EC configuration and PV-B-EC configuration during a double day and single night cycle. The operating voltage and current of the EC are designed $V_{EC}$ and $I_{EC}$ in both the PV-EC and PV-B-EC configurations shown in Fig. 6. In this figure, each day is compressed into one hour, followed by an extended night period of approximately two hours. In the PV-EC configuration, both current and voltage follow the irradiance pattern displayed in Fig. 1b. From morning to noon, the current density increases by a factor of five (7 to 35 mA cm$^{-2}$), with the voltage varying by approximately 1.0 V. In the PV-B-EC configuration, the operating points of the EC remain relatively constant irrespective to the irradiance. From morning to noon and during the night, EC current density ranges between 8 mA cm$^{-2}$ to 13 mA cm$^{-2}$ with a voltage gradient of only 0.12 V.

The power coupling factor in either configuration is a measure of what fraction of the maximum power deliverable by the PV is being utilized. In PV-EC, the load is the EC and in PV-B-EC, the load is B-EC. In PV-EC, the coupling factor varies between 0.75 and 1 with peak values near "noon" when PV power output is the highest. In the PV-B-EC configuration, the power coupling efficiency remains high between 0.95 and 1 during daytime. The addition of the battery not only allowed continuous EC day and night operation, but also stabilized EC operating voltage, current and power throughout daytime despite irradiance fluctuation and the day-and-night cycle. Fig. S4 in the SI presents the operating power of the EC in the PV-EC configuration in comparison with PV-B-EC.

Electrochemical (EC) faradaic efficiency consistently favored CO across all current–voltage conditions examined in this work. During PV-EC operation on day 1, $H_2$ faradaic efficiency was 7% at the start of the day when the operating voltage ($V_{OP}$) was low, decreased to 6% at midday when $V_{OP}$ reached its maximum, and returned to 8% by the end of the day. A similar trend was observed on day 2, with $H_2$ selectivity starting at 14%, dropping to 8% at midday, and rising to 19% by the end of the day.

In contrast, during PV-B-EC operation using the same Ag-GDE, where the operating voltage remained nearly constant, $H_2$ faradaic efficiency increased steadily from 19% at the beginning of day 1 to 34% by the end of day 2, including the overnight period. These results highlight two key observations: first, the current–voltage profile influences EC selectivity, with $H_2$ formation minimized at higher voltages and currents (midday conditions). This dependence of the product selectivity on voltage has been observed in other studies.[56–59] Second, even though CO remains the predominant product in our work, $H_2$ selectivity gradually increases over time. This has been observed in our previous work[33] and was attributed to the initial high hydrophobicity of the freshly prepared Ag gas-diffusion electrode (Ag-GDE). In a flow cell, electrolyte access to the catalyst surface is indispensable for $CO_2$ reduction; however, excessive wetting undermines CO selectivity by promoting the hydrogen evolution reaction (HER) and possible flooding of the GDE.[60] Hydrophobicity limits electrolyte (1 M $KHCO_3$) contact with the catalyst surface, but with continued operation, exposure to ionic species such as $OH^-$, $HCO_3^-$, and $K^+$, as well as potential salt accumulation, progressively reduces the hydrophobic character of the Ag-GDE.[55,61]

This increase water availability (from electrolyte) at the triple-phase boundary, thereby promoting hydrogen evolution *via* water reduction. To determine whether the observed selectivity is associated with microstructural changes in the silver particles caused by dynamic *versus* constant voltage profiles, their morphology and structural phase were examined in a dedicated experiment using scanning transmission electron microscopy (STEM) and 4D-STEM.

## Microstructural analysis of Ag nanoparticles under fluctuating *versus* constant voltage operation

To study the influence of the operating conditions on the catalyst microstructure, we conducted a dedicated experiment in an H-cell using silver nanoparticles deposited on TEM finder grids. From a total of three TEM grids (Grid 1, Grid 2, and Grid 3), Grid 1 supported pristine silver nanoparticles without electrochemical utilization. Silver nanoparticles subjected to a 10-minute electrochemical process in the H-cell were deposited on Grid 2 under dynamic voltage (simulating PV-EC operation), and on Grid 3 under constant voltage (simulating PV-B-EC operation). The fabrication workflow and experimental setup are illustrated in Fig. S5 and S6 of the SI, and the corresponding current–voltage characteristics are shown in Fig. S7.

All three TEM grids were characterized using scanning transmission electron microscopy (STEM) and four-dimensional scanning transmission electron microscopy (4D-STEM). Fig. 7 presents STEM secondary electron and dark-field images of Grid 1 (Fig. 7a), Grid 2 (Fig. 7b), and Grid 3 (Fig. 7c). Across all grids, the silver nanoparticles, whether pristine, subjected to dynamic voltage, or subjected to constant voltage, appear agglomerated with inhomogeneous shapes and particle sizes ranging from 50 to 200 nm. Occasionally, elongated flake- or chip-like protrusions are observed in all three samples.

(a) Grid 1: Pristine Ag

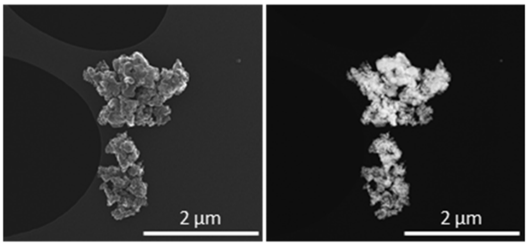

(b) Grid 2: Ag under dynamic voltage

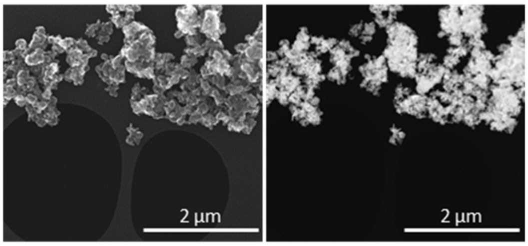

(c) Grid 3: Ag under constant voltage

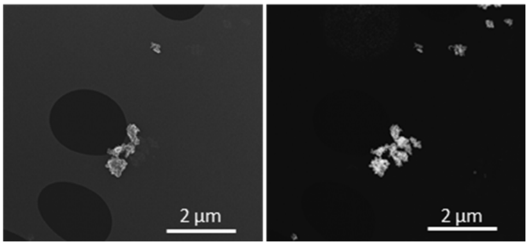

Fig. 7 STEM images of silver nanoparticles. (a) Secondary electron image on the right and dark field image on the left of pristine silver nanoparticles deposited on grid 1, (b) secondary electron image on the right and dark field image on the left of silver nanoparticles deposited on grid 2 employed for the electrochemical process under a dynamic voltage profile, and (c) secondary electron image on the right and dark field image on the left of silver nanoparticles deposited on grid 3 employed for the electrochemical process under a constant voltage profile.

Notably, no drastic changes in the appearance and surface topology of the silver nanoparticles (50–200 nm) are observed when comparing the pristine catalyst with those used for $CO_2$ reduction under either dynamic or constant voltage conditions.

After electrolysis under both constant and dynamic voltage conditions, both grids occasionally exhibited regions containing ensembles of aggregates of smaller particles, predominantly below 10 nm in size; this can be seen in Fig. S8 in the SI. While small-nanoparticle formation was not predominant, it may become increasingly relevant during prolonged operation, with the present observations capturing its early onset.

The generation of small Ag nanoparticles after the $CO_2RR$ under constant voltage has previously been reported in identical-location studies by Yun *et al.*[62] The newly formed smaller particle aggregates observed in Grid 2 and Grid 3 were further investigated by energy-dispersive X-ray spectroscopy (EDX) (Fig. S8), which confirmed the presence of silver under both voltage protocols. Following this confirmation, the aggregates were analyzed using 4D-STEM (Fig. 8) to identify the structural phases of silver and assess the potential influence of electrochemical operating conditions on the particle structure.

The experimentally obtained diffraction patterns from particle aggregates in Grid 2, formed after electrolysis under dynamic voltage, and Grid 3, formed after electrolysis under constant voltage, were compared with simulated crystallographic reference patterns for cubic metallic silver, silver(I) oxide, silver fluoride, and silver chloride. Among these, metallic silver and silver oxide are considered the most plausible phases, given the metallic nature of the commercial silver catalyst and the possibility of partial oxidation over time. The presence of silver fluoride may be attributed to the intrinsic fluorine content of the TEM grids, while silver chloride could originate from trace chloride contamination in the H-cell electrolyte. The reference patterns and corresponding phase assignments are shown in Fig. 8, where dark blue indicates metallic silver, red indicates silver oxide, light blue indicates silver fluoride, and light orange indicates silver chloride. In small particle aggregate regions, the diffraction signatures were most frequently consistent with metallic silver, with occasional areas showing patterns compatible with silver oxide. In contrast, diffraction features consistent with AgF and AgCl were observed only rarely and with substantially lower occurrence in both grids.

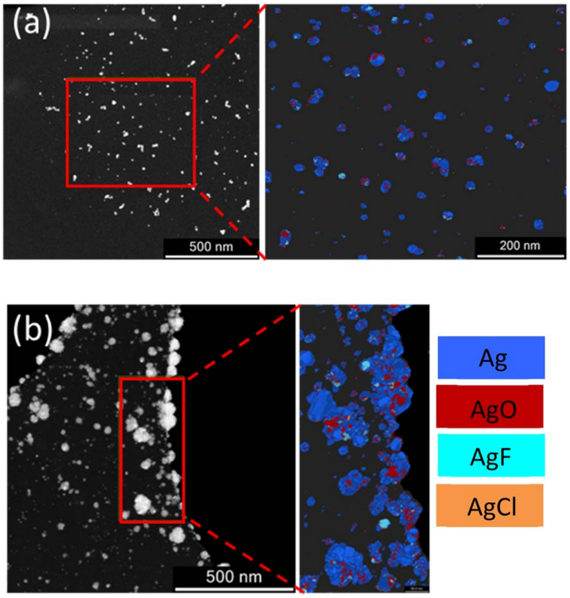

Fig. 8 4D-STEM images of smaller particle aggregates and their corresponding phase assignments, obtained by comparison with reference diffraction patterns of metallic silver (dark blue), silver oxide (red), silver fluoride (green), and silver chloride (orange). (a) Particles on Grid 2 after electrochemical processing under dynamic voltage. (b) Particles on grid 3 after electrochemical processing under constant voltage.

The selectivity obtained with the flow cell in the PV-EC and PV-B-EC experiments is distinct, although CO remains the dominant product in both cases. However, we find no decisive evidence that this difference in selectivity originates from changes in microstructural features or in the silver oxidation state under either dynamic or constant voltage profiles. For Grid 2 and Grid 3, despite a current variation of approximately five-fold in grid 2, the overall morphology, surface texture of the silver particles, and the emergence of smaller Ag particle sizes are remarkably similar. This observation highlights the structural resilience of the Ag catalyst, independent of the applied voltage–current profile during the 10 min H-cell experiment. Preserving catalyst structure is generally desirable, as it helps maintain targeted active-site characteristics and can therefore sustain catalytic activity and selectivity.[63] Based on these observations, we propose that selectivity differences emerging on short time scales are likely governed by macroscopic effects, such as gas-diffusion electrode (GDE) flooding or salt deposition on the membrane or within the GDE, both of which are well documented in flow-cell $CO_2$ electrolysis systems.

In our recent work on Ag-GDE efficiency in PV-EC systems under realistic field irradiance and temperature profiles, we highlighted the importance of developing cathodes that retain high selectivity despite the unavoidable broad variations in current density encountered in practical operation.[33] Here, we demonstrate PV-B-EC as an effective strategy to mitigate current density fluctuations and reduce the operating voltage, enabling continuous electrolysis during both day and night. Consequently, operation in a PV-B-EC configuration substantially relaxes the requirement for cathodes to sustain high selectivity across wide current density ranges.

## Energy balance comparison between PV-EC and PV-B-EC in double-day, single night cycles

The energy balance presented in this section evaluate the efficiency of converting a one-day photovoltaic energy output into

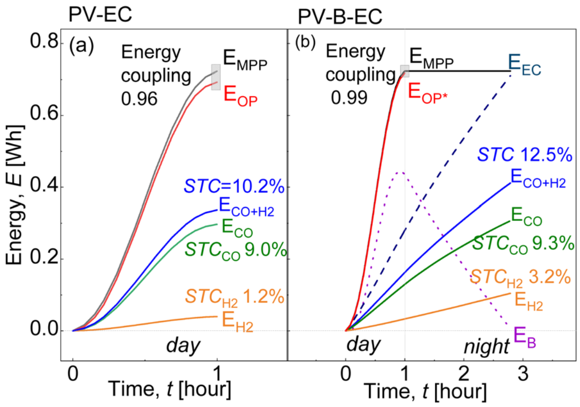

Fig. 9 Temporal evolution of cumulative energies involved in each step of the solar-to-chemical conversion efficiency of a single day PV output for the two scenarios: (a) PV-EC and (b) PV-B-EC.

chemicals. In both device configurations, the Ag-GDE in the electrochemical cell was unchanged. To minimize the influence of the catalyst age when evaluating the system performance, we compared day 2 of the PV-EC experiment with day 1 + long night on PV-B-EC. With identical PV area and efficiency in PV-EC and PV-B-EC configurations, Fig. 9a and b show identical cumulative maximum attainable PV energies, 0.722 Wh. As shown in Fig. 9a, EC is the only load, and its operating energy reached 0.69 Wh, representing a remarkable energy coupling factor of 0.96, on par with values achieved with maximum power point trackers.[64] As shown in Fig. 9b, with a parallelly connected load B and EC load, the cumulative operating energy at the end of day 1 is 0.716 Wh, corresponding to an energy coupling of 0.99. This value is higher than that achieved in the PV-EC configuration and exceeds typical values obtained with a maximum power point tracker across a broad range of PV power inputs (from 0.2 sun to 1.1 sun). This remarkable result aligns with our previous observations of improved coupling efficiency.[46–48] PV-B-EC combinations are therefore a very attractive option for PV-storage integration, addressing timescales from hours to seasons with a high degree of intrinsic operational stability without any active control.

In the PV-EC configuration (Fig. 9a), the cumulative sun energy stored using the EC through $CO_2$ reduction into CO and hydrogen evolution ($H_2$ and CO) was 0.330 Wh, corresponding to total solar-to-chemical efficiency of 10.0%. Solar-to-chemical $H_2$ efficiency ($STC_{H_2}$) was 1.0% and solar-to-chemical CO efficiency ($STC_{CO}$) was 9.0%. In contrast, in the PV-B-EC configuration (Fig. 9b), the PV energy stored in the battery on day 1 is utilized by the EC during the subsequent night. Therefore, to evaluate STC of the PV-B-EC system, the energy balance must encompass both day 1 and the following night. Across the entire day–night cycle of PV-B-EC operation, the cumulative sun energy stored through chemical formation (CO and $H_2$) was 0.394 Wh or a STC of 12.5% with a $STC_{H_2}$ of 3.2% and a $STC_{CO}$ of 9.3%.

Table 1 summarizes the efficiencies of the PV-EC and PV-B-EC systems. A high coupling factor helps prevent mismatches between PV generation and EC demand while minimizing electrical losses during PV energy storage. The photovoltaic module exhibited an energy efficiency of 21.9% over the day of operation. The EC component was identical in both configurations; however, its efficiency was higher in the PV-B-EC system (57.8%) compared to the PV-EC system (47.5%). The inclusion of a battery led to a more stable EC operating voltage, maintaining it around 2.5 V, whereas in the PV-EC configuration, the voltage fluctuated with irradiance between 2.4 V and 3.2 V. Consequently, in the PV-B-EC configuration, the EC utilized PV energy more effectively by operating at a steadier and lower power level over a longer duration.

Table 1 Comparison of PV-EC and PV-B-EC system efficiency in terms of energy coupling efficiency and solar-to-chemical efficiency (CO and $H_2$)

| | PV-EC | PV-B-EC |
|---|---|---|
| Photovoltaic efficiency | 21.9% | 21.9% |
| Energy coupling factor | 0.96 | 0.99 |
| Electrochemical cell efficiency | 47.5 ± 4.7% | 57.8 ± 3.2% |
| Solar-to-chemical efficiency (STC) | 10.2 ± 1.0% | 12.5 ± 0.7% |
| $STC_{CO}$ | 9.0 ± 0.8% | 9.3 ± 0.3% |
| $STC_{H_2}$ | 1.20 ± 0.4% | 3.20 ± 0.5% |

This effect arises because the battery stores a portion of the PV power that would otherwise be immediately consumed by the EC in a PV-EC system and releases it later, enabling continued EC operation during nighttime. With the nearly optimal coupling factor and higher EC efficiency achieved in the PV-B-EC system, the overall solar-to-chemical efficiency was 2.3%$_{abs.}$ higher than that of the PV-EC system (57.8% *vs.* 47.5%). Due to the increased $H_2$ selectivity in the PV-B-EC configuration, the solar-to-chemical efficiency toward $H_2$ improved from 1.2% to 3.2%. Although CO selectivity was lower in the battery-assisted EC compared to the standalone EC, the solar-to-chemical efficiency toward CO ($STC_{CO}$) still increased by 0.3% $_{abs.}$ as a result of improved coupling and voltage efficiency. In $CO_2$ reduction, the hydrogen evolution reaction (HER) is typically a competing pathway that reduces product selectivity. In the present study, although the improved solar-to-chemical (STC) efficiency partially reflects increased hydrogen production, it is important to note that mixed CO and $H_2$ streams (syngas) are relevant for a range of downstream processes, including Fischer–Tropsch synthesis, methanol synthesis and anaerobic fermentation, where specific $CO:H_2$ ratios are required. In this context, our previous work demonstrates that electrochemical systems can flexibly tune $CO:H_2$ ratios to match downstream requirements.[65] Accordingly, STC efficiency is retained as a meaningful system-level metric for evaluating overall solar energy conversion.

## Analysis of the results, synergy in B-EC operation and efficiency beyond the limit

In our previous work, we investigated a simplified on/off operating cycle with a rectangular time profile and single-product electrolysis ($H_2$ from water splitting).[46–48] This controlled setup was necessary to isolate the differences between PV-EC and PV-EC-B operation and to evaluate efficiency with minimal uncertainty. In the present study, we advance to a more complex and realistic scenario involving $CO_2$ reduction under field-relevant PV operating conditions. The increased complexity arises from the introduction of two products (CO and $H_2$) and from the dynamic irradiance-temperature effects on both EC and EC-B configurations. Despite these added layers, the results remain qualitatively consistent with our previous findings.[46–48] While the electrochemical aspect of the study is presented above, in this section we delve into the details of the operating performance. The simple parallel connection of a battery to a PV-EC device has been theoretically and experimentally demonstrated[46,47] to have three key aspects: Firstly, the PV-EC-B device is capable of self-sustained operation without the need for power conversion or matching electronics, providing stable, smooth input EC power throughout the day/night cycle. Secondly, the battery facilitates effective power coupling in the PV-EC-B device by stabilising the operating voltage. Thirdly, the battery distributes PV energy over a longer period of time, delivering this energy at a lower power to the EC compared to a system without a battery. This is beneficial to electrolyser efficiency and therefore to the total STC of the whole PV-EC-B device.[46–48]

As demonstrated in the previous sections, all three points have been confirmed in realistic operating cycle tests. This is the next milestone in the development of simple and efficient hybrid storage solutions for integration with PV at the module, string or field level, before the inverter. This concept is vital for the early stabilisation of PV output and the smooth deployment of PV in a grid rich in renewable generation.

The third aspect, the efficiency boost facilitated by the battery, is of particular interest and has been addressed in detail in previous work. This boost in efficiency is synergistic and is observed despite battery losses because these losses are subtracted from, rather than added to, the energy losses in the EC device.[46,47] This boost has been predicted theoretically and demonstrated experimentally,[46,47] and has been used to show that the solar-to-hydrogen efficiency of a PV-EC-B system can be 1.9% higher than the theoretical efficiency limit of an equivalent PV-EC system in an idealised operating cycle.[48] In this study, we examine these effects under a realistic operating cycle and analyse how they compare to the results obtained under idealised on/off operating conditions. To do so, we first determine the efficiency limit of the PV-EC reference system. We employ our recently developed reverse analysis procedure, designed for the rapid evaluation of solar-to-chemical efficiency in PV-driven electrolysers.[66] This method extends earlier work originally developed for evaluating solar-to-hydrogen efficiency in PV-driven water-splitting electrolisers.[67] The updated version has been generalised to systems that produce multiple products and accounts for variations in the main factors that determine the power input to the EC device: the PV efficiency ($\eta_{\mathrm{p}}$□), the irradiance (G), and the PV-to-EC area ratio ($A_{\mathrm{R}}$). These system parameters, together with the known EC output characteristics, define the solar-to-chemical efficiency that the electrolyser can achieve when paired with any PV device, under any irradiance, at any PV-to-EC area scaling, and with any mode of power coupling. The resulting value defines the efficiency limit of the ideally coupled PV-EC system. Importantly, this implicit solution does not require system simulation; instead, it is derived through straightforward mathematical transformations. Using the EC polarization curves as the input and the corresponding partial current densities for CO and $H_2$ as the output, we calculated the maximum achievable solar-to-chemical efficiency ($\mathrm{STC}_{\mathrm{limit}}$) for the given PV device and PV-to-EC area ratio for the range of irradiance covered in the experiment. In the calculations of $\mathrm{STC}_{\mathrm{limit}}$, a coupling factor of 1 is assumed, as direct coupling is in principle capable of approaching 100% of maximum PV power transfer to EC with marginal loss in electric connections. Fig. 10 presents $\mathrm{STC}_{\mathrm{limit}}$ as filled circles (black for CO + $H_2$, blue for CO, and grey for $H_2$) as a function of solar irradiance, G, for constant PV efficiency $\eta_{\mathrm{PV}} = 22.09\%$ and PV-to-EC area ratio $A_{\mathrm{R}} = 4.87$. The experimentally measured $\mathrm{STC}_{\mathrm{CO}}$ and $\mathrm{STC}_{\mathrm{H_2}}$ over the course of a single day are shown as blue and black hollow circles, respectively.

As shown in Fig. 10, the hyperbolic decrease in $\mathrm{STC}_{\mathrm{limit}}$ with increasing irradiance arises from the fundamental dependence of the EC voltage efficiency on the EC operating voltage. As irradiance increases, the PV delivers a higher operating voltage to the EC device. However, the EC voltage efficiency exhibits a hyperbolic decline with increasing operating voltage; this dependence is shown in Fig. S9 in the SI. Since the $\mathrm{STC}_{\mathrm{limit}}$ is directly proportional to the EC voltage efficiency, it consequently inherits this hyperbolic decay. At low irradiance, the measured STC of the PV-EC device lies substantially below the attainable limit due to coupling losses under low-power operating conditions (see Fig. 6a). At higher irradiances, from approximately 600 W $\mathrm{m}^{-2}$ and above, the measured $\mathrm{STC}_{\mathrm{CO+H_2}}$, $\mathrm{STC}_{\mathrm{H_2}}$ and $\mathrm{STC}_{\mathrm{CO}}$ of the PV-EC device approach their respective limits, causing the trends to converge. This represents the maximum performance regime, where the power coupling is close to its ideal value. The slight overshoot of the experimental values above the limit line arises from variations in the EC input and output characteristics during the measurements. The limit calculations are representative of the state of the EC characteristics from 2.30 V to 3.25 V. Any variation in these characteristics affects the limit line. Here, we demonstrate that the PV-EC-B hybrid can exceed the limit of the equivalent PV-EC system by a significant amount under realistic field utilisation scenarios. As shown in Fig. 10, STC increases by 2.3%abs. above the PV-EC reference limit. The battery-assisted system exceeds this reference system-efficiency limit because the battery decouples PV power generation from instantaneous EC conversion, allowing the same solar energy to be converted at a lower EC power density.

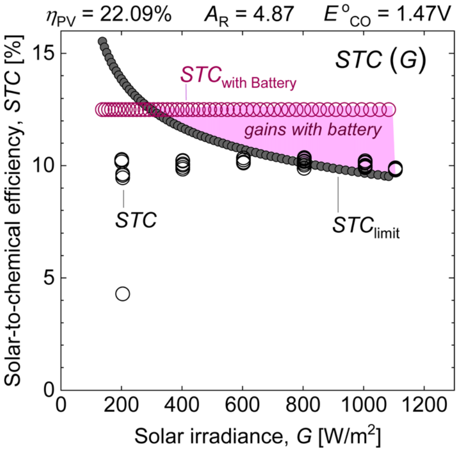

Fig. 10 Comparison between the theoretical solar-to-chemical efficiency limit ($\mathrm{STC}_{\mathrm{limit}}$) calculated for the EC using $\eta_{\mathrm{PV}} = 22.09\%$ and a PV-to-EC area ratio ($A_{\mathrm{R}}$) of 4.87, and the experimentally measured total solar-to-chemical efficiencies (CO + $H_2$). The calculated $\mathrm{STC}_{\mathrm{limit}}$ values (CO + $H_2$) are shown as black filled circles, while the measured STC values for the PV-EC configuration are indicated by black hollow circles. The measured STC values for the PV-B-EC device (pink hollow circles) exceed the $\mathrm{STC}_{\mathrm{limit}}$ achievable by the PV-EC reference system.

In the SI (Fig. S10), the measured STC values and the corresponding theoretical limits are presented separately for CO and $H_2$.

This feature of the EC-B hybrid can be exploited in two ways: either as a direct increase in product yield, or to reduce the size of the costly EC component while retaining the same efficiency as its PV-EC counterpart with a larger EC. In our research on water splitting, we demonstrated that approximately a twofold reduction in EC capacity can be achieved.[48] While the extent of EC downsizing under realistic operating conditions remains to be fully quantified, these results provide a clear indication of the potential and direction for further investigation.

## Solar-to-chemical efficiency in Si-PV driven electrochemical $CO_2$ reduction: benchmarking and insights

The solar-to-chemical efficiency depends on the PCE of the PV device, coupling and efficiency of the electrolyser. In this study, we selected silicon-based PV technology due to its widespread adoption, making it the most practical candidate for large-scale photovoltaic-driven $CO_2$ reduction. In systems comparable to ours (Si-PV coupled with a GDE flow-type EC cell),[68–70] the electrochemical cell efficiency ($\eta_{EC}$) for CO and $H_2$ production typically ranges between 40% and 50%.

Strategies to enhance $\eta_{EC}$ include operating at lower voltage and consequently low current density,[71] optimizing the anode and cathode for reduce overpotentials, and improving the EC architecture to minimize ohmic losses such as through zero-gap cell design.[72] At low operating voltages and current densities, the EC potential approaches the thermoneutral potential of the targeted reactions, leading to high voltage efficiency. However, for practical applications, achieving a high STC at relevant current densities remains the key challenge. For instance, Arai *et al.* reported an impressive $\eta_{EC}$ 57%[71] but only at 1.5 mA cm$^{-2}$ while Sriramagiri *et al.* presented a large silicon PV-EC system operating with an $\eta_{EC}$ of 42% at a current density of 40 mA cm$^{-2}$, the highest current density reported for the same class of device. In our Si-PV coupled with the GDE flow-type EC cell, $\eta_{EC}$ ranged from 60% to 46% across current densities from 7.2 mA cm$^{-2}$ to 35 mA cm$^{-2}$ during daytime operation. Integration of a battery further improved $\eta_{EC}$ to 52% and 60% by extending the EC operation period while maintaining a stable and lower operating voltage, approx. 2.5 V, and current density in the range of 8.3 to 12.6 mA cm$^{-2}$, as shown in Fig. 11.

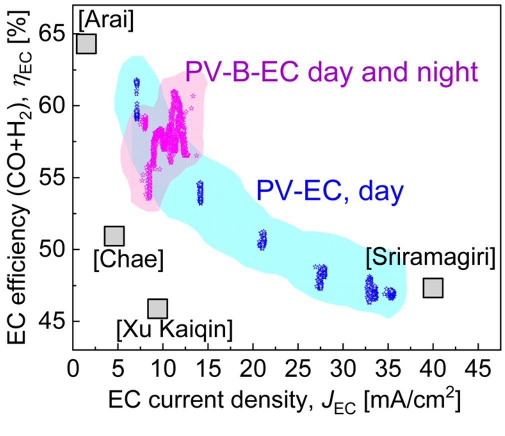

Fig. 11 Comparison of electrochemical cell efficiency over specific current density for relevant Si-PV-flow type EC systems in the literature [68–71] and in this work (with and without the aid of a battery).

The simple addition of a commercial Li-ion battery increased EC efficiency, leading to an improvement in solar-to-chemical efficiency from 10.2% to 12.5% under the same solar energy input. This study demonstrates that integrating a battery can serve as a powerful strategy to enhance PV-EC system performance, improving solar-to-chemical conversion efficiency without requiring complex or costly modifications to the PV or EC components. This represents an important milestone in optimizing photovoltaic energy utilization under realistic, intermittent operating conditions. The battery-assisted configuration enables stable and self-sustained solar energy storage through continuous fuel production at lower and more stable EC operating power, thereby contributing to $CO_2$ emission mitigation and advancing the practicality of solar-driven chemical energy systems.

## Conclusion

We investigated the conversion of solar energy into chemical fuels *via* the $CO_2$RR under realistic daily irradiance and temperature conditions using two direct-coupled system configurations: a direct photovoltaic–electrochemical system (PV-EC) and a photovoltaic–battery–electrochemical system (PV-B-EC). In both cases, the PV modules of same active area exposed to same solar irradiance and temperature profile had a total maximally attainable electricity output of 0.722 Wh. In the PV-EC system, the power coupling factor (C) fluctuated between 0.75 and 1, reaching its maximum during periods of peak PV output. In contrast, the PV-B-EC configuration retained a consistently high C value (0.95–1) regardless of environmental variations. By the end of daytime operation, the energy coupling factor of the PV-EC system was 0.96, whereas that of the PV-B-EC system reached 0.99. This enhanced stability resulted from the battery's ability to buffer PV power fluctuations with minimal deviation in operating voltage. The integration of the battery extended the electrolysis runtime enabling the EC system to convert daily PV energy at steadier and lower power compared with the PV-EC configuration and resulting in a 2.3%$_{abs.}$ increase in solar-to-chemical (STC) efficiency. Using a reverse analysis, we show that the PV-B-EC hybrid exceeds the theoretical PV-EC efficiency limit, confirming a synergistic boost from battery-mediated voltage stabilization. This effect persists under realistic operating conditions and can be leveraged to increase product yield or reduce electrolyser size while retaining efficiency. Scanning transmission electron microscopy (STEM) and four-dimensional STEM (4D-STEM) analyses show no significant microstructural or phase differences between silver particles operated under stabilized and dynamic voltage–current conditions. While our previous work highlighted the need for cathodes to maintain high selectivity under the broad current density variations inherent to PV-EC operation under realistic field conditions, the present results demonstrate that PV-B-EC mitigates these fluctuations, lowers the operating voltage, and enables continuous day-and-night electrolysis. Consequently, the requirement for cathodes to sustain selectivity across wide current density ranges is substantially relaxed.

PV-B-EC systems present a promising, scalable route for day–night solar fuel production, mitigating both short-term variability and long-term intermittency in solar power. This work reframes the role of batteries in solar-to-fuel technologies, not as costly, oversized storage devices, but as precision components that unlock greater efficiency, stability, and year-round performance in photovoltaic-driven chemical conversion.

## Author contributions

This work was a collaborative effort. Thérèse Cibaka contributed to conceptualization, experimental investigation, data analysis, writing – original draft, and manuscript editing. Tsvetelina Merdzhanova and Oleksandr Astakhov contributed to supervision, conceptualization, definition of research objectives, analysis of NREL PV module data, and the determination of realistic irradiance and temperature conditions for a representative summer day, as well as writing and manuscript editing. Robert Zandonella contributed to the development and design of the original TEM grid setup, STEM and 4D-STEM analysis of Ag particles before and after H-cell $CO_2$ reduction, and manuscript editing. Sergey Shcherbachenko contributed to adapting the emulator algorithm, measuring *I–V* curves of the silicon heterojunction PV module under varying irradiance and temperature conditions, and manuscript editing. Paul Paciok contributed to discussions on the interpretation of STEM data and to manuscript editing. Marc Heggen contributed to supervision, provision of STEM facilities, and manuscript editing. Rafal Dunin-Borkowski and Christoph Brabec contributed to the provision of equipment and material resources and manuscript editing. Peter Strasser contributed to supervision, formal analysis, and manuscript editing.

## Conflicts of interest

There are no conflicts to declare.

## Data availability

The data supporting this article have been included as part of the supplementary information (SI) and available for download under the following link: https://fz-juelich.sciebo.de/s/nEHwCNALRcQCRnb. Supplementary information is available. See DOI: https://doi.org/10.1039/d6el00076b.

## Acknowledgements

The authors would like to thank Joachim Kirchhoff and Daniel Weigand for their technical support in building the $CO_2$ reduction setup and constructing the PV-B-EC setup, Viktor Schlichting for the support with battery characterization and PV-B-EC setup construction, Ugochi Chime for the silicon heterojunction PV cell preparation and *I–V* curve measurements, and Lars Wieprecht for the daily laboratory support. This work made use of Research Center Juelich facilities, and the authors express gratitude to the HITEC program for funding. The authors gratefully acknowledge the European Commission under the SUPERVAL Project (Grant agreement no. 101115456).

## References

1 P. Bojek, *Energy-system/Renewables/Solar-pv*, https://www.iea.org/energy-system/renewables/solar-pv.
2 E. O'Shaughnessy, J. R. Cruce and K. Xu, *Sol. Energy*, 2020, **208**, 1068–1077.
3 B. Frew, B. Sergi, P. Denholm, W. Cole, N. Gates, D. Levie and R. Margolis, *Joule*, 2021, **5**, 1143–1167.
4 G. N. Psarros, P. A. Dratsas, P. P. Chinaris and S. A. Papathanassiou, *ApEn*, 2025, 381.
5 U. Datta, A. Kalam and J. Shi, *Energy Storage*, 2021, **3**, e224.
6 U. Chibuko, T. Merdzhanova, D. Weigand, F. Ezema, S. Agbo, U. Rau and O. Astakhov, *Sol. Energy*, 2023, **249**, 233–241.
7 S. Shcherbachenko, O. Astakhov, U. Chime, L.-C. Kin, K. Ding, B. Pieters, U. Rau, E. Figgemeier and T. Merdzhanova, *Sol. RRL*, 2022, **7**, 2200857.
8 R. Nematirad, A. Pahwa and B. Natarajan, *Solar*, 2024, **4**, 179–208.
9 G. Squadrito, G. Maggio and A. Nicita, *Renewable Energy*, 2023, 216.
10 A. Risco-Bravo, C. Varela, J. Bartels and E. Zondervan, *Renewable Sustainable Energy Rev.*, 2024, **189**, 113930.
11 B. S. Zainal, P. J. Ker, H. Mohamed, H. C. Ong, I. M. R. Fattah, S. M. A. Rahman, L. D. Nghiem and T. M. I. Mahlia, *Renewable Sustainable Energy Rev.*, 2024, **189**, 113941.
12 M. E. Ivanova, R. Peters, M. Muller, S. Haas, M. F. Seidler, G. Mutschke, K. Eckert, P. Rose, S. Calnan, R. Bagacki, R. Schlatmann, C. Grosselindemann, L. A. Schafer, N. H. Menzler, A. Weber, R. van de Krol, F. Liang, F. F. Abdi, S. Brendelberger, N. Neumann, J. Grobbel, M. Roeb, C. Sattler, I. Duran, B. Dietrich, M. E. C. Hofberger, L. Stoppel, N. Uhlenbruck, T. Wetzel, D. Rauner, A. Hecimovic, U. Fantz, N. Kulyk, J. Harting and O. Guillon, *Angew Chem. Int. Ed. Engl.*, 2023, **62**, e202218850.
13 G. Segev, J. Kibsgaard, C. Hahn, Z. J. Xu, W.-H. Cheng, T. G. Deutsch, C. Xiang, J. Z. Zhang, L. Hammarström, D. G. Nocera, A. Z. Weber, P. Agbo, T. Hisatomi, F. E. Osterloh, K. Domen, F. F. Abdi, S. Haussener, D. J. Miller, S. Ardo, P. C. McIntyre, T. Hannappel, S. Hu, H. Atwater, J. M. Gregoire, M. Z. Ertem, I. D. Sharp, K.-S. Choi, J. S. Lee, O. Ishitani, J. W. Ager, R. R. Prabhakar, A. T. Bell, S. W. Boettcher, K. Vincent, K. Takanabe, V. Artero, R. Napier, B. R. Cuenya, M. T. M. Koper, R. Van De Krol and F. Houle, *J. Phys. D: Appl. Phys.*, 2022, **55**, 323003.
14 G. Gurudayal, J. Bullock, D. F. Srankó, C. M. Towle, Y. Lum, M. Hettick, M. C. Scott, A. Javey and J. Ager, *Energy Environ. Sci.*, 2017, **10**, 2222–2230.
15 C. Ampelli, D. Giusi, M. Miceli, T. Merdzhanova, V. Smirnov, U. Chime, O. Astakhov, A. J. Martín, F. L. P. Veenstra, F. A. G. Pineda, J. González-Cobos, M. García-Tecedor, S. Giménez, W. Jaegermann, G. Centi, J. Pérez-Ramírez,

J. R. Galán-Mascarós and S. Perathoner, *Energy Environ. Sci.*, 2023, **16**, 1644–1661.

16 Y. Xiao, Y. Qian, A. Chen, T. Qin, F. Zhang, H. Tang, Z. Qiu and B.-L. Lin, *J. Mater. Chem. A*, 2020, **8**, 18310–18317.

17 C. R. Cox, J. Z. Lee, D. G. Nocera and T. Buonassisi, *Proc. Natl. Acad. Sci. U. S. A.*, 2014, **111**, 14057–14061.

18 S. Esiner, J. Wang and R. A. J. Janssen, *Cell Rep. Phys. Sci.*, 2020, **1**, 100058.

19 A. Mohammadi and M. Mehrpooya, *Energy*, 2018, **158**, 632–655.

20 M. Reuß, J. Reul, T. Grube, M. Langemann, S. Calnan, M. Robinius, R. Schlatmann, U. Rau and D. Stolten, *Sustainable Energy Fuels*, 2019, **3**, 801–813.

21 N. G. Chatzigeorgiou, S. Theocharides, G. Makrides and G. E. Georghiou, *J. Energy Storage*, 2024, **86**, 111192.

22 M. Arunachalam and D. S. Han, *Emergent Mater.*, 2024, 1–15.

23 S. N. Agbo, T. Merdzhanova, S. C. Yu, H. Tempel, H. Kungl, R. A. Eichel, U. Rau and O. Astakhov, *J. Power Sources*, 2016, **327**, 340–344.

24 S. N. Agbo, T. Merdzhanova, S. Yu, H. Tempel, H. Kungl, R.-A. Eichel, U. Rau and O. Astakhov, *Phys. Status Solidi A*, 2016, **213**, 1926–1931.

25 K. Y. Khouzam, *ITEnC*, 1990, **5**, 265–271.

26 K. Khouzam, L. Khouzam and P. Groumpos, *Sol. Energy*, 1991, **46**, 101–108.

27 S. Paul Ayeng'o, H. Axelsen, D. Haberschusz and D. U. Sauer, *SoEn*, 2019, **183**, 120–131.

28 Y. Shi, T.-Y. Hsieh, M. A. Hoque, W. Cambarau, S. Narbey, C. Gimbert-Surinach, E. Palomares, M. Lanza and A. Llobet, *ACS Appl. Mater. Interfaces*, 2020, **12**, 55856–55864.

29 T. L. Gibson and N. A. Kelly, *Int. J. Hydrogen Energy*, 2008, **33**, 5931–5940.

30 R. E. Clarke, S. Giddey, F. T. Ciacchi, S. P. S. Badwal, B. Paul and J. Andrews, *Int. J. Hydrogen Energy*, 2009, **34**, 2531–2542.

31 T. Maeda, H. Ito, Y. Hasegawa, Z. Zhou and M. Ishida, *Int. J. Hydrogen Energy*, 2012, **37**, 4819–4828.

32 E. Kemppainen, S. Aschbrenner, F. Bao, A. Luxa, C. Schary, R. Bors, S. Janke, I. Dorbandt, B. Stannowski, R. Schlatmann and S. Calnan, *Sustainable Energy Fuels*, 2020, **4**, 4831–4847.

33 T. Cibaka, T. Merdzhanova, O. Astakhov, S. Shcherbachenko, G. Liu, C. v. Pham, U. Rau and P. Strasser, *Energy Fuels*, 2026, **40**(1), 811–818.

34 N. Kakimoto and R. Asano, *IEEE Trans. Sustain. Energy*, 2017, **8**, 1647–1657.

35 W. Li, H.-C. Fu, Y. Zhao, J.-H. He and S. Jin, *Chem*, 2018, **4**, 2644–2657.

36 S. Shcherbachenko, O. Astakhov, U. Chime, L.-C. Kin, K. Ding, B. Pieters, U. Rau, E. Figgemeier and T. Merdzhanova, *Sol. RRL*, 2023, **7**, 2200857.

37 O. Astakhov, T. Merdzhanova, L.-C. Kin and U. Rau, *Sol. Energy*, 2020, **206**, 732–740.

38 S. N. Agbo, T. Merdzhanova, S. C. Yu, H. Tempel, H. Kungl, R. A. Eichel, U. Rau and O. Astakhov, *Phys. Status Solidi A*, 2016, **213**, 1926–1931.

39 J. Brillet, J.-H. Yum, M. Cornuz, T. Hisatomi, R. Solarska, J. Augustynski, M. Graetzel and K. Sivula, *Nat. Photonics*, 2012, **6**, 824–828.

40 J. Jia, L. C. Seitz, J. D. Benck, Y. Huo, Y. Chen, J. W. Ng, T. Bilir, J. S. Harris and T. F. Jaramillo, *Nat. Commun.*, 2016, **7**, 13237.

41 W. J. Chang, K. H. Lee, H. Ha, K. Jin, G. Kim, S. T. Hwang, H. M. Lee, S. W. Ahn, W. Yoon, H. Seo, J. S. Hong, Y. K. Go, J. I. Ha and K. T. Nam, *ACS Omega*, 2017, **2**, 1009–1018.

42 M. Lee, X. Ding, S. Banerjee, F. Krause, V. Smirnov, O. Astakhov, T. Merdzhanova, B. Klingebiel, T. Kirchartz, F. Finger, U. Rau and S. Haas, *Adv. Mater. Technol.*, 2020, **5**, 2000592.

43 H. Park, I. J. Park, M. G. Lee, K. C. Kwon, S. P. Hong, D. H. Kim, S. A. Lee, T. H. Lee, C. Kim, C. W. Moon, D. Y. Son, G. H. Jung, H. S. Yang, J. R. Lee, J. Lee, N. G. Park, S. Y. Kim, J. Y. Kim and H. W. Jang, *ACS Appl. Mater. Interfaces*, 2019, **11**, 33835–33843.

44 J. He and C. Janaky, *ACS Energy Lett.*, 2020, **5**, 1996–2014.

45 I. E. L. Stephens, K. Chan, A. Bagger, S. W. Boettcher, J. Bonin, E. Boutin, A. K. Buckley, R. Buonsanti, E. R. Cave, X. Chang, S. W. Chee, A. H. M. da Silva, P. de Luna, O. Einsle, B. Endrődi, M. Escudero-Escribano, J. V. Ferreira de Araujo, M. C. Figueiredo, C. Hahn, K. U. Hansen, S. Haussener, S. Hunegnaw, Z. Huo, Y. J. Hwang, C. Janáky, B. S. Jayathilake, F. Jiao, Z. P. Jovanov, P. Karimi, M. T. M. Koper, K. P. Kuhl, W. H. Lee, Z. Liang, X. Liu, S. Ma, M. Ma, H.-S. Oh, M. Robert, B. R. Cuenya, J. Rossmeisl, C. Roy, M. P. Ryan, E. H. Sargent, P. Sebastián-Pascual, B. Seger, L. Steier, P. Strasser, A. S. Varela, R. E. Vos, X. Wang, B. Xu, H. Yadegari and Y. Zhou, *J. Phys. Energy*, 2022, **4**, 042003.

46 O. Astakhov, S. N. Agbo, K. Welter, V. Smirnov, U. Rau and T. Merdzhanova, *J. Power Sources*, 2021, **509**, 230367.

47 L.-C. Kin, O. Astakhov, M. Lee, S. Haas, K. Ding, T. Merdzhanova and U. Rau, *Sol. RRL*, 2022, **6**(4), 2100916.

48 U. Chibuko, T. Merdzhanova, S. Agbo, U. Rau, U. Wurstbauer and O. Astakhov, *Int. J. Hydrogen Energy*, 2025, **127**, 38–50.

49 M. F. Seidler, B. Pieters, W. Zwaygardt, S. Haas, O. Astakhov and T. Merdzhanova, *J. Power Sources*, 2025, **641**, 236723.

50 U. Chime, L. Wolf, V. Buga, D. Weigand, A. Gad, J. Köhler, A. Lambertz, W. Duan, K. Ding, T. Merdzhanova, U. Rau and O. Astakhov, *Sol. RRL*, 2022, **6**, 2100594.

51 A. A. W. Marion, C. Deline, S. Glick, M. Muller, G. Perrin, J. Rodriguez, S. Rummel, K. Terwilliger and T. J. Silverman, *User's Manual for Data for Validating Models for PV Module Performance*, Report NREL/TP-5200-61610, National Renewable Energy Laboratory (NREL), 2014.

52 B. Marion, M. G. Deceglie and T. J. Silverman, *Sol. Energy*, 2014, **110**, 736–744.

53 M. E. Leonard, L. E. Clarke, A. Forner-Cuenca, S. M. Brown and F. R. Brushett, *ChemSusChem*, 2020, **13**, 400–411.

54 A. Angulo, P. van der Linde, H. Gardeniers, M. Modestino and D. Fernández Rivas, *Joule*, 2020, **4**, 555–579.

55 K. Krause, J. K. Lee, C. Lee, H. W. Shafaque, P. J. Kim, K. F. Fahy, P. Shrestha, J. M. LaManna, E. Baltic, D. L. Jacobson, D. S. Hussey and A. Bazylak, *J. Power Sources*, 2022, **520**, 230879.

56 C. Luan, Y. Shao, Q. Lu, S. Gao, K. Huang, H. Wu and K. Yao, *ACS Appl. Mater. Interfaces*, 2018, **10**, 17950–17956.

57 M. Valenti, N. P. Prasad, R. Kas, D. Bohra, M. Ma, V. Balasubramanian, L. Chu, S. Gimenez, J. Bisquert, B. Dam and W. A. Smith, *ACS Catal.*, 2019, **9**, 3527–3536.

58 Y.-C. Hsieh, S. D. Senanayake, Y. Zhang, W. Xu and D. E. Polyansky, *ACS Catal.*, 2015, **5**, 5349–5356.

59 M. Ma, B. J. Trześniewski, J. Xie and W. A. Smith, *Angew. Chem., Int. Ed.*, 2016, **55**, 9748–9752.

60 K. Yang, R. Kas, W. A. Smith and T. Burdyny, *ACS Energy Lett.*, 2021, **6**, 33–40.

61 C. Ampelli, F. Tavella, D. Giusi, A. M. Ronsisvalle, S. Perathoner and G. Centi, *Catal. Today*, 2023, **421**, 114217.

62 H. Yun, J. Kim, W. Choi, M. H. Han, J. H. Park, H.-s. Oh, D. H. Won, K. Kwak and Y. J. Hwang, *Electrochim. Acta*, 2021, **371**, 137795.

63 R. M. Arán-Ais, Y. Yu, R. Hovden, J. Solla-Gullón, E. Herrero, J. M. Feliu and H. D. Abruña, *J. Am. Chem. Soc.*, 2015, **137**, 14992–14998.

64 S. Shcherbachenko, O. Astakhov, U. Chime, L.-C. Kin, K. Ding, B. Pieters, U. Rau, E. Figgemeier and T. Merdzhanova, *Sol. RRL*, 2022, **7**, 2200857–2200865.

65 F. L. P. Veenstra, T. Cibaka, A. J. Martin, D. Weigand, J. Kirchhoff, V. Smirnov, T. Merdzhanova and J. Perez-Ramirez, *ChemSusChem*, 2024, **17**, e202301398.

66 O. Astakhov, T. Cibaka, L. Wieprecht, U. Rau and T. Merdzhanova, *ChemSusChem*, 2024, e202402027, DOI: 10.1002/cssc.202402027.

67 O. Astakhov, V. Smirnov, U. Rau and T. Merdzhanova, *Sol. RRL*, 2022, **6**, 2100783.

68 S. Y. Chae, S. Y. Lee, S. G. Han, H. Kim, J. Ko, S. Park, O. S. Joo, D. Kim, Y. Kang, U. Lee, Y. J. Hwang and B. K. Min, *Sustainable Energy Fuels*, 2020, **4**, 199–212.

69 G. M. Sriramagiri, N. Ahmed, W. Luc, K. D. Dobson, S. S. Hegedus and F. Jiao, *ACS Sustain. Chem. Eng.*, 2017, **5**, 10959–10966.

70 K. Xu, S. Ning, H. Chen, S. Ouyang, J. Wang, L. Song, J. Lv and J. Ye, *Sol. RRL*, 2020, **4**, 2000116.

71 T. Arai, S. Sato, K. Sekizawa, T. M. Suzuki and T. Morikawa, *Chem. Commun.*, 2019, **55**, 237–240.

72 L. Hoof, N. Thissen, K. Pellumbi, K. junge Puring, D. Siegmund, A. K. Mechler and U.-P. Apfel, *Cell Rep. Phys. Sci.*, 2022, **3**, 100825.